A Portable Magnetometer for Magnetic Measurements of Meter-Sized Meteorites

Elise Clavé, Clara Maurel, Eduardo Lima, Jay Shah, Elias Mansbach, Minoru Uehara, Benjamin Weiss

Geochemistry, Geophysics, Geosystems

RESEARCH ARTICLE
10.1029/2020GC009266

A Portable Magnetometer for Magnetic Measurements of Meter-Sized Meteorites

Elise Clavé[1,2], Clara Maurel[1], Eduardo A. Lima[1], Jay Shah[1], Elias N. Mansbach[1], Minoru Uehara[3], and Benjamin P. Weiss[1]

[1]Department of Earth, Atmospheric and Planetary Sciences, Massachusetts Institute of Technology, Cambridge, MA, USA, [2]Institut Supérieur de l'Aéronautique et de l'Espace, ISAE-SUPAERO, Toulouse Cedex, France, [3]Aix Marseille Univ, CNRS, IRD, INRAE, Coll France, CEREGE, Aix-en-Provence, France

Elise Clavé and Clara Maurel contributed equally.

Key Points:

- Understanding planetary remanent magnetism benefits from measurements at spatial scales ranging from hand samples to global maps
- We designed a portable magnetometer array and data processing that allows on-site magnetic measurements of up to meter-size objects
- This system enables estimation of the net magnetic moment of some of the largest known meteorites on Earth

Correspondence to:
E. Clavé,
clave955@gmail.com

Citation:
Clavé, E., Maurel, C., Lima, E. A., Shah, J., Mansbach, E. N., Uehara, M., et al. (2020). A portable magnetometer for magnetic measurements of meter-sized meteorites. *Geochemistry, Geophysics, Geosystems*, *21*, e2020GC009266. https://doi.org/10.1029/2020GC009266

Received 1 JUL 2020
Accepted 29 SEP 2020

Abstract Meteorites contain records of past magnetic fields in the form of natural remanent magnetization (NRM). A key property of meteorite magnetization that provides information about its origin is its dependence on spatial scale. In particular, understanding how the mean remanent magnetization varies from the scale of meteorites to the global scale of their parent bodies would aid in the interpretation of spacecraft magnetometry data. However, the vast majority of meteorite samples whose remanent magnetization have been measured have sizes <10 cm due to the limited size range accommodated by laboratory magnetometers. To address this limitation, we developed a portable magnetometer array that enables remanence measurements of meter-size meteorites in a non-magnetically shielded environment. The instrument measures both NRM and induced magnetization using two orthogonal square Helmholtz coil pairs that compensate the vertical and horizontal components of the background magnetic field. An array of four magnetometers mounted on a movable aluminum rail measures the magnetic field at multiple locations around the sample. The instrument is transportable and can be adapted to different sample sizes. After distinguishing the induced component from the remanent component of a sample's total field, the remanence can be estimated from a multipole field inversion combined with nonlinear least squares method. We validated the instrument and data processing on a magnet of known magnetic moment and measured the NRM of a meter-sized iron meteorite.

Plain Language Summary Meteorites are remnant fragments of planetary bodies. Their physical properties reflect the history of their environment and that of on their parent bodies. In particular, some meteorites preserve records of past magnetic fields experienced on their parent asteroids in the form of natural remanent magnetization. This remanence can be probed by spacecraft magnetometers to infer the intensity and direction of ancient magnetizing fields. However, it is unclear how to relate global scale measurements of planetary magnetization to that of meteorites measured in the laboratory. A major limitation is that the scaling of meteorite magnetization with size is largely unknown. Establishing such scaling requires measuring the remanent magnetizations of larger and larger meteorites. However, nearly all meteorites previously analyzed were typically smaller than ~10 cm in diameter owing to the limited size and portability of the instruments. To facilitate the measurements of larger meteorites, we designed and built a portable instrument that enables measurements of the remanent and induced magnetizations of meter-size meteorites at their storage location. We validated the instrument performance against a sample of known magnetic moment and then used it to measure a large iron meteorite.

1. Introduction

The NASA Discovery mission Psyche plans to orbit the asteroid (16) Psyche in 2026 and measure its magnetic field (Elkins-Tanton et al., 2017). With an estimated mean radius of 113 km (Shepard et al., 2017) and mean density of 3,700 ± 300 kg m^{-3}, (16) Psyche is estimated to contain up to 60 vol. % metal (Elkins-Tanton et al., 2020), making it the largest known metal-rich body in the solar system. A leading hypothesis to explain the asteroid's metal-rich composition is that it is the iron core of an ancient protoplanet. This protoplanet likely would have undergone several energetic impacts, stripping away most of its rocky mantle (Asphaug & Reufer, 2014). The energy deposited by the impacts could have melted the core and the subsequent advection

of this conductive fluid could have powered a dynamo, generating a magnetic field magnetizing the solid outermost layers of the body (Neufeld et al., 2019; Weiss et al., 2010). This hypothesis will be supported if the Psyche spacecraft's fluxgate Magnetometer detects a substantial remanent magnetic field (Polanskey et al., 2018).

Past magnetic fields are recorded by planetary materials in the form of remanent magnetization (i.e., remanent magnetic moment per unit mass, A m^2 kg^{-1}). Remanent magnetization reflects the semi-permanent alignment of electron spins within the object's constituent ferromagnetic grains. Remanent magnetization is typically sensed by measuring its magnetic field using a magnetometer outside the sample. This field depends on the orientation and intensity of the magnetization throughout the body, which in turns depend on the ferromagnetic minerals present, their crystal sizes, and the processes by which they were magnetized. For example, the average magnetization of a uniformly-magnetized object remains constant as its volume increases, while the average magnetization decreases with increasing volume if the object is composed of blocks whose magnetizations are collectively randomly oriented. As a consequence, the magnetic field of an object cannot be readily predicted based on knowledge of its size and fine-scale magnetization alone. This is in stark contrast to the gravity field, which instead is a function of a scalar property (mass density) that is shared by all materials, thereby enabling first-order predictions for the planetary gravity field as a function of body size (e.g., Ermakov et al., 2018).

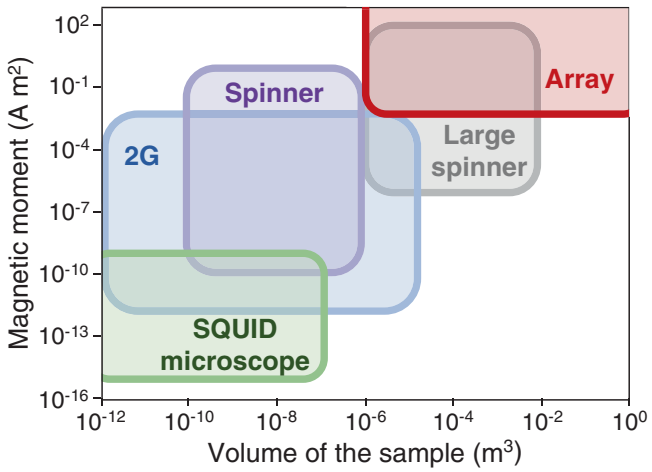

Figure 1. Ranges of detectable magnetic moment and volume of the sample accommodated by various magnetometers. The maximum magnetic moment that can be estimated with the superconducting quantum interference device (SQUID) microscope (Weiss et al., 2007) was calculated assuming a dipole field of 40 μT measured at a distance of 500 μm. For the 2G Enterprises Superconducting Rock Magnetometer (Fuller et al., 1985), the maximum magnetic moment is dictated by the saturation level of the field sensors. The detectable magnetic moments for the spinner magnetometer are given by the manufacturer Advanced Geoscience Instruments Company for the model JR-6. For the large spinner magnetometer, the minimum and maximum magnetic moments are calculated using a minimum and maximum detectable dipole field by the fluxgate of 1 nT at 10 cm and 100 μT at 30 cm, respectively (Uehara et al., 2017). The minimum sample size that we have measured with our array is ~1 cm, although the instrument could in principle be adapted to detect smaller samples. The minimum magnetic moment corresponds to a case where the field components are below the fluxgate detection limit of 1 nT in more than 25% of the positions for the medium-size instrument presented in this paper; this limit could potentially be lowered, for example, by decreasing the sensor-to-sample distance. Our instrument could be readily adapted to accommodate larger volumes and estimate larger magnetic moments.

The Psyche Magnetometer is designed to detect fields between ~0.2 nT and ~80,000 nT (Polanskey et al., 2018). The sensitivity and dynamic range of the Magnetometer are defined by simulating Psyche's magnetic field using uniformly magnetized spherical volumes with known magnetization directions. The predicted remanent field strengths critically depend on the size and number of these consitutent spheres and the strength of their individual magnetic moments (e.g., Biersteker et al., 2019). However, nearly all existing laboratory magnetometry measurements have only measured meteorite subsamples $\lesssim$90 cm^3 in volume (i.e., with effective diameter $\lesssim$10 cm and typical mass $\lesssim$1 kg; Terho et al., 1993). However, there exist hundreds of iron meteorites weighing >10 kg that could be analyzed magnetically to determine the dependence of magnetization scale on size (Buchwald, 1975).

To this end, we developed a portable magnetometer array and associated data processing software that enable estimation of magnetic moments of meter-size meteorites outside the laboratory to uncertainties of better than a factor of ~2. Simple modifications to our instrument should enable measurements of samples of any size, so long as coils can be placed around it. For the configuration of the instrument presented in this paper, magnetic moments from ~10^{-2} to at least 400 A m^2 can be estimated. Both lower and upper limits mainly depend on the size of the system, the resolution of the sensors used and the sensor-to-sample distance. The magnetometer array measures the magnetic field resulting from the sample's total magnetization. The total magnetization is the sum of the induced magnetization and a remanent magnetization. The magnetic moment is then estimated using a nonlinear least-squares multipole inversion of the portion of the field produced by the remanent magnetization only.

Depending on the sensitivity required, magnetic measurements of mm- and cm-size meteorite samples are typically acquired using superconducting or spinner magnetometers in a magnetically-shielded environment (Figure 1; Fuller et al., 1985; Uehara et al., 2017; Weiss et al., 2007). However, none of these instruments are designed to accommodate meter-size samples. Magnetic moments of larger objects such as spacecraft (Mehlem, 1978) and meteorites of volume ~0.1 m^3 (Wasilewski et al.,

2002) have been estimated when the samples could be brought to the measurement site. On the other hand, our instrument was specifically designed for large meteorites that cannot be moved outside their storage location or cannot be subsampled: it is transportable, can be assembled in less than a day and does not require magnetic shielding.

The instrument is described in Section 2 and its theory of operation is explained in Section 3. Section 4 presents a test case in which we estimate the magnetization of a well-characterized sample. We also describe the sources of uncertainty in our measurements and how we take them into account in the final estimates. In Section 5, we present the measurements of an iron meteorite's magnetization.

2. Description of the Magnetometer Array

2.1. Architecture

The requirement of making measurements without magnetic shielding presents a major challenge not typically encountered when using smaller laboratory magnetometers (Figure 1). In addition to contributing measurement noise from temporal flucutations, the background magnetic field at the measurement site introduces a secondary component to the magnetization of the sample, which results in an induced field that contributes to the total magnetic field of the sample. To isolate the constant remanent component of the sample's total field from the induced component, our instrument exposes the sample to fields of controlled intensities.

The instrument consists of a two-axis square Helmholtz coil system whose main axes are oriented vertically and horizontally (Figure 2). The frames of the coils and their support structure are composed of nonmagnetic aluminum rails, available in different lengths (10, 15, 30, 60, and 120 cm) and which can be combined to obtain the desired coil size. The rails are attached with nonmagnetic aluminum brackets and nylon screws and bolts. The coils are wound with enameled 18 American wire gauge copper wire. To facilitate the winding of the coils, the wire is taped to the coil frames. Each set of two coils is wired in series and powered by a separate output of a BK Precision 9130 power supply operated in constant current mode. The sample is placed at the center of the system on a rigid nonmagnetic mounting. In total, five commercial three-axis fluxgate magnetometers are used: four Macintyre Electronic Design Associates (MEDA) FVM400s to sense the sample's field and one Bartington Instruments Mag-03MS100 for measurements of the applied field. The MEDA fluxgates are rigidly attached to a movable aluminum rail and the distance between the fluxgates is

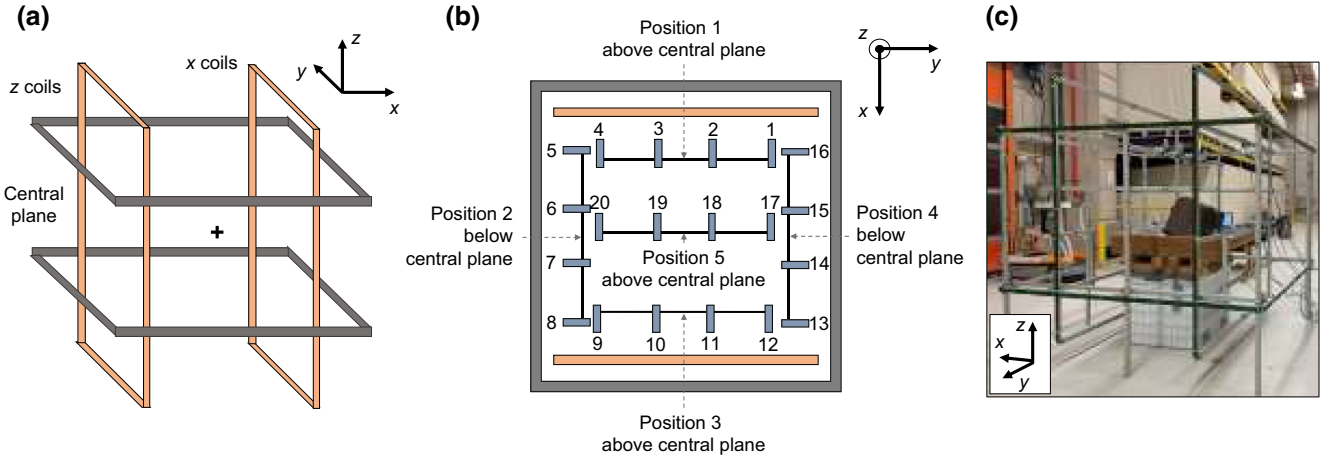

Figure 2. Schematic and picture of the magnetometer array. (a) Three-dimensional view. The origin of the reference frame is indicated by the cross at the center of the system, the central plane is shown in gray. The system is manually oriented such that the background field vector is contained in the *x*–*z* plane. The gray and orange rectangles represent the horizontal and vertical coils, respectively. (b) Top view with five sequential positions of the movable rail (black lines) above and below the central plane. The blue rectangles represent the fluxgates on the rail. Fluxgates locations are numbered from 1 to 20. The gray and orange rectangles represent the horizontal and vertical coils, respectively. (c) Picture of the two-axis square Helmholtz coil system at the storage facility of the Smithsonian Museum of Natural History. The coils are wrapped with green wire. The Casas Grandes IIIAB iron meteorite (Section 5) is at the center of the system and the rail is in position 5.

chosen so that there is no crosstalk (>15 cm). As much as possible, they should be placed away (~20 cm) from the Helmoltz coils when the rail is in place to avoid saturation of the fluxgates in this region where generated fields are > 250 μT. While the rail may be placed anywhere inside the system, preference should be given to positions that maximize the measurement spatial coverage. During our experiments, we placed the rail at five different positions: four positions on each side of the sample above and below the horizontal central plane, and one above the sample (Figure 2). When no sample is inside the system, the Bartington fluxgate is located at the center of the coil system and is employed in the adjustment of the compensating field. In the following, the z axis denotes the vertical axis of the coils and the x axis denotes the horizontal one, with the y axis completing the right-handed triad (Figure 2). The origin of the reference frame is taken at the center of the system.

Data acquisition with the MEDA fluxgates consists of 30-s-long signals recorded at a 17.4-Hz sampling frequency. The electronics boxes of the MEDA fluxgates are directly connected to the computer through RS232 connectors. The Bartington magnetometer's sampling frequency is 625 Hz. This magnetometer is connected to the computer through a signal processing unit (SCU-3, Bartington Instruments), a four-channel 24-bit analog-to-digital converter unit (NI9239, National Instruments) and a universal serial bus chassis (NI cDAQ-9174). A LabVIEW virtual instrument (VI) controls the magnetometers through serial port communication for the MEDA instruments and a DAQ Assistant for the Bartington. The VI simultaneously records and saves the raw data acquired by all the magnetometers. Prior to any subsequent data processing, the raw data acquired with the Bartington fluxgate are downsampled by only keeping the points of the time series that match the sampling frequency of the MEDA fluxgates. The gain of all fluxgates was set to 1.

2.2. Generation of a Controlled Magnetic Field

When electric currents run through the coils, the Helmholtz coil system generates a magnetic field in the direction following Faraday's law of induction. The intensity of the field and its spatial uniformity are functions of the number of coils, their size and relative location, the number of wire turns and the current applied to the coils. Helmholtz coils were selected for two practical reasons: they only consist of two coils, which facilitates the system's transportation and assembly, and their performance is relatively insensitive to deviations from the theoretical configuration, unlike other systems such as the Merritt four-coil systems (Kirschvink, 1992). Square coils were chosen because they are much easier to build and store than circular coils.

The field applied at the center of the two sets of coils $\left(\vec{B}_{\text{applied}}\right)$ is the sum of the background field $\left(\vec{B}_{\text{bg}}\right)$ and the compensation field generated by the coils $\left(\vec{B}_{\text{comp}}\right)$:

$$\vec{B}_{\text{applied}} = \vec{B}_{\text{bg}} + \vec{B}_{\text{comp}} \tag{1}$$

To provide partial or total suppression of the uncontrolled background field, the compensation field and the background field must be antiparallel. Otherwise, only part of the compensation field will contribute to controlling the magnitude of the applied field. In the two-axis Helmholtz coil system, $\vec{B}_{\text{comp}}$ is in the $y = 0$ plane (Figure 2). We must therefore orient the system (and its reference frame) to ensure that $\vec{B}_{\text{bg}}$ is also in the $y = 0$ plane. The whole system is manually rotated until the Bartington fluxgate placed at the center indicates that the component of the background field along y is minimal. Manual imprecision and temporal fluctuations of the background field act against a perfect alignment of the horizontal components and the resulting uncertainties are taken into account in the postprocessing of the data (Section 4). The orientation of $\vec{B}_{\text{comp}}$ within the $y = 0$ plane is controlled by the respective currents running through the z and x coil systems.

2.3. Adjusting the System Parameters to a Given Sample and Environment

We designed the magnetometer array to address (1) constraints of sample size, space, time, and resources allocated for the measurements, (2) transportability, and (3) variability of the background field on site.

The sample size dictates the minimum volume of the region in which the compensation field must be uniform, which depends on the size of the coils. The coil size in turn determines the distance between the coils for the Helmholtz configuration (Kirschvink, 1992) as well as the wire turns. The number of wire turns for the x and z coils controls the maximum intensity of the compensation field for a given current. Given that winding the coils is the most time-consuming step of the assembly, the number of wire turns can be adjusted to the minimum required to compensate the background field up to a chosen level. It is important to confirm that the power supply can deliver the desired current and the wire gauge used can properly dissipate the heat generated by ohmic losses. The measurements are repeated for increasing input current (i.e., compensation field intensity) from 0 A to the maximum current selected. The number of positions of the fluxgate rail mainly depends on the time available for the experiment. It dictates the number of data points and the spatial coverage; as a consequence, it may influence the accuracy of estimated magnetic moment. In practice, we have found (Section 4) that the 20 locations spaced on average by ∼30° adopted here (Figure 2) are sufficient to estimate the magnetic moment of a small magnet to within ∼5% of its nominal value.

To choose the system parameters, we simulated the compensation field generated by the coil system. For this, we computed the magnetic field generated at any point in space by a current in a rectangular loop of wire (Misakian, 2000). For a square loop centered on the origin of the $z = 0$ plane, the three components of the compensation field at a given point of coordinates (x, y, z) are:

$$
\begin{aligned}
B_{\mathrm{comp},X}(x,y,z) &= \frac{\mu_0 I}{4\pi}\sum_{i=1}^{4}\frac{(-1)^{i+1}z}{r_i\left(r_i+b_i\right)}\\
B_{\mathrm{comp},Y}(x,y,z) &= \frac{\mu_0 I}{4\pi}\sum_{i=1}^{4}\frac{(-1)^{i+1}z}{r_i\left(r_i+(-1)^{i+1}a_i\right)}\\
B_{\mathrm{comp},Z}(x,y,z) &= \frac{\mu_0 I}{4\pi}\sum_{i=1}^{4}\left[\frac{(-1)^{i}b_i}{r_i\left(r_i+(-1)^{i+1}a_i\right)}-\frac{a_i}{r_i\left(r_i+b_i\right)}\right]
\end{aligned}
\tag{2}
$$

where $(a_i, b_i, 0)$ are the coordinates of the corners of the coil (i= 1, 2, 3, 4), r_i is the distance in m between corner i of the loop and the point (x, y, z), μ_0 (H m^{-1}) is the vacuum permeability and I (A) is the current running clockwise through the loop (Misakian, 2000). We sum the magnetic fields generated by each electrical loop of the two sets of coils after having translated and rotated the field vectors to match the configuration of the actual system. The system's parameters can be varied in the simulation to obtain the desired total compensation field where the sample is located during the experiment (Figure 3).

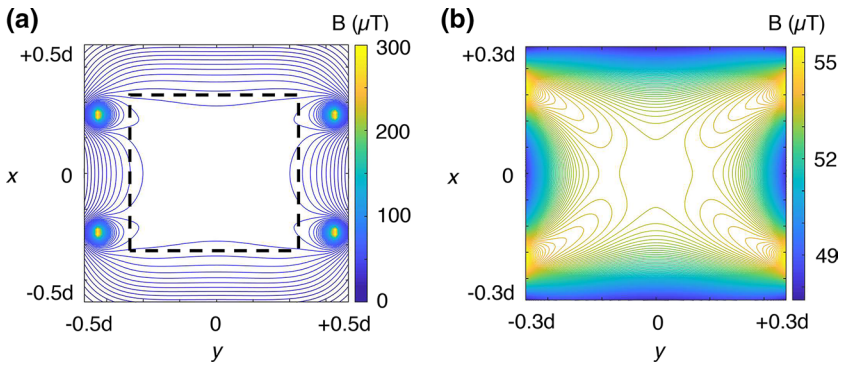

Figure 3. Simulation of the magnitude of compensation field in the $z = 0$ plane of a two-axis square Helmholtz coil system. (a) Contour plot of the field intensity inside the z coils with length d. The four areas of high field strength are at the intersections of the x coils with the central plane (x coils are inside the z coils). Dashed area is plotted in (b). (b) Contour plot of the field intensity inside the central area of the system where the field is most uniform.

Before assembling the coils, the background field must be measured close to where the sample will be located. Based on the strength of the background field, the simulation enables the determination of the number of wire turns required for each coil. Once the coils are assembled and the structure positioned, the currents running through the x and z coils are varied to find the values that reduce the applied field to a minimum (zero or otherwise, depending on the capacity of the power supply). The data processing requires making measurements at several intermediate current values between 0 A and the maximum value. The ratio of the current values in the x and z coils, which can be computed from the simulations, must be constant at each step to ensure that the compensation field is always aligned with the background field.

The time required for assembling and using the system depends on its size and, in particular, on the number of wire turns needed to compensate the background field. For example, with two people, coils of size 1.5 m and about 15 wire turns (Section 4) take ~1 h to be assembled and ~1.5 h to be wound. Coils of size 2.5 m and about 25 wire turns (Section 5) take ~6 h to be assembled and wound. Depending on the size of the system, aligning its reference frame with the background field can take up to 30 min. For meter-size meteorites (Section 5) bringing and centering the sample inside the system could take up to 30 min. Finally, a complete series of measurements take ~2.5 h. For small samples (e.g., requiring coils < 1 m), one could consider upgrading the system to make it collapsible for transportation. This would avoid having to rewind the coils at every location visited.

3. Theory of Operation

Here we describe the protocol for estimating a sample's remanent magnetic moment using field measurements conducted with and without the sample. The following sections present the successive data processing steps to obtain the magnetic moment.

3.1. Sequence of Measurements for the Different Fields of Interest

For a given position of the fluxgate rail, two 30-s data acquisitions (Section 2.1) are conducted for each current step and averaged. Measurements at no current ($I = 0$ A) are taken in the first and last steps of the series to account for variations in the background field. The rail is sequentially moved to the other positions and the measurements are conducted again. This whole sequence is first performed without the sample and then again with the sample centered in the system. Without the sample, the Bartington sensor is placed at the center of the system to provide a reference value of the background field; the applied field is obtained by adding to the background field the simulated values of the compensation field generated for each current step (Equation 1, Figure 4a). The measurements conducted at each position (x, y, z) of the other fluxgates are concatenated into $\vec{B}_{\text{total}}^{\text{no sample}}$ (Figure 4b). These values will be subtracted from the corresponding ones obtained with the sample inside $\left(\vec{B}_{\text{total}}^{\text{with sample}}\right)$ and averaged to estimate the sample's total field:

$$\vec{B}_{\text{sample}} = \vec{B}_{\text{total}}^{\text{with sample}} - \vec{B}_{\text{total}}^{\text{no sample}} \tag{3}$$

The difference between $\vec{B}_{\text{total}}^{\text{no sample}}$ and $\vec{B}_{\text{applied}}$ is that the former is measured at each position of the fluxgates while the latter is measured at the center of the system.

3.2. Isolation of the Sample's Remanent Field

The sample's total field is the sum of its remanent $\left(\vec{B}_{\text{rem}}\right)$ and induced component $\left(\vec{B}_{\text{ind}}\right)$:

$$\vec{B}_{\text{sample}} = \vec{B}_{\text{ind}} + \vec{B}_{\text{rem}} \tag{4}$$

The induced field is produced by a magnetic moment, $\vec{m}_{\text{ind}}$, induced in the sample by the applied field. The vector $\vec{m}_{\text{ind}}$ is related to $\vec{B}_{\text{applied}}$ via the volume magnetic susceptibility ($\underline{\chi}$, unitless in SI), a second-rank

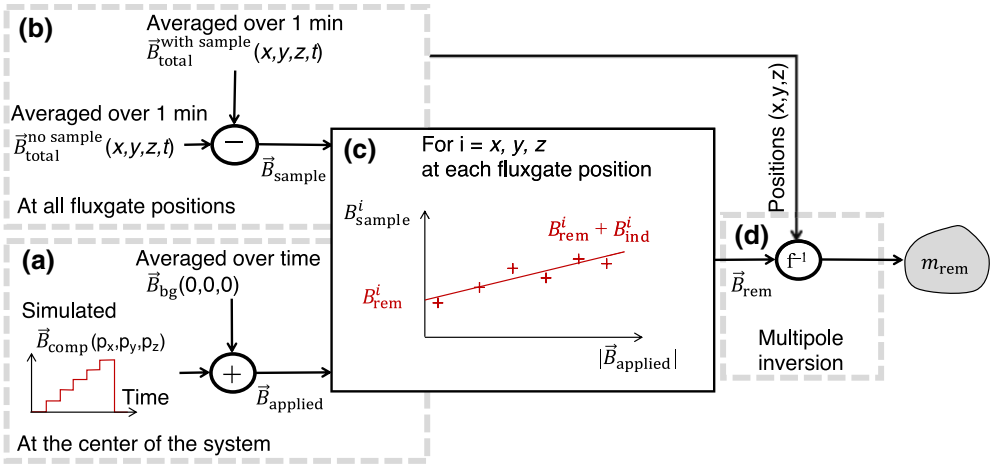

Figure 4. Data processing flow. The four boxes (a–d) illustrate the four main steps of the protocol. (a) The field applied to the sample is estimated by adding the average of (1) the background field measured at the center of the system without sample and for $I = 0$ A and (2) the compensation field at a random point (p_x, p_y, p_z) within the volume of the sample obtained by simulation for each current step (Equation 1, Sections 3.1 and 3.4). (b) In parallel, the sample's total field is obtained by subtracting the measurements of the field inside the system with and without the sample, averaged over the acquisition time, for each fluxgate position and each current values (Section 3.1). (c) The three components of the sample's remanent field are found for each fluxgate position at the intercept of the regression line fitting the values of the sample's total field plotted against the magnitude of the applied field (Section 3.2). (d) A multipole inversion of the remanent field provides an estimate of the remanent magnetic moment of the sample (Section 3.3).

tensor that characterizes the strength of the magnetic response of a material to an external field (Tauxe et al., 2018). $\underline{\chi}$ can be approximated by a scalar if the induced magnetization in the sample lies close to the applied field direction. However, for natural samples such as iron meteorites whose anisotropy of susceptibility can range from a few percent to 300% (Gattacceca et al., 2005), we retain $\underline{\chi}$ in tensor form. We denote $\hat{r}_{\text{applied}}$ the unit radial vector in the direction of the applied field such that $\vec{B}_{\text{applied}} = B_{\text{applied}}\hat{r}_{\text{applied}}$, with B_{applied} the magnitude of the applied field. We can write:

$$\vec{m}_{\text{ind}} = \frac{V}{\mu_0}\underline{\chi}B_{\text{applied}}\hat{r}_{\text{applied}} \tag{5}$$

where V (m^3) is the volume of the sample. Approximating the induced field of the sample as that of a dipole (i.e., assuming the distance between the center and the magnetic source r is sufficiently large), we have:

$$\vec{B}_{\text{ind}} = \frac{V}{4\pi r^3}B_{\text{applied}}\left\{\frac{3\left[\vec{r}\cdot\left(\underline{\chi}\hat{r}_{\text{applied}}\right)\right]}{r^2}\vec{r} - \underline{\chi}\hat{r}_{\text{applied}}\right\} \tag{6}$$

Each component of the induced field is proportional to the magnitude of the applied field; the proportionality factors are functions of the magnetic susceptibility of the material, the position where the measurement is made, and the orientation of the applied field (Equation 6). Therefore, for a constant applied field direction, each component of $\vec{B}_{\text{sample}}$ is a linear function of B_{applied}, which is controlled and measured. For all positions of the fluxgates, each component of $\vec{B}_{\text{sample}}$ is plotted against B_{applied}. The intercept of a regression line fitting these data provides the corresponding component of $\vec{B}_{\text{rem}}$ (Figure 4c), which is independent from the susceptibility.

3.3. Estimation of the Magnetic Moment

To estimate the magnetic moment of the sample (Figure 4d), we take advantage of the fact that any magnetic field produced by sources distributed within a finite volume can be described in the form of a spherical harmonic expansion (Cain et al., 1967):

$$
\begin{aligned}
B_r &= \sum_{n=1}^{N}\left(\frac{a}{r}\right)^{n+2}(n+1)\sum_{k=0}^{n}\left[g_n^k\cos(k\phi)+h_n^k\sin(k\phi)\right]P_n^k(\theta)\\
B_\theta &= -\sum_{n=1}^{N}\left(\frac{a}{r}\right)^{n+2}\sum_{k=0}^{n}\left[g_n^k\cos(k\phi)+h_n^k\sin(m\phi)\right]\frac{\partial P_n^k(\theta)}{\partial\theta}\\
B_\phi &= \frac{1}{\sin\theta}\sum_{n=1}^{N}\left(\frac{a}{r}\right)^{n+2}\sum_{k=0}^{n}k\left[g_n^k\sin(k\phi)+h_n^k\cos(k\phi)\right]P_n^k(\theta)
\end{aligned}
\tag{7}
$$

In Equation 7, (r,θ,ϕ) are the spherical coordinates of the sensors with respect to the origin of the expansion (r_0,θ_0,ϕ_0); B_r, B_θ, B_ϕ are the three components of the measured magnetic field; a is the radius of a reference sphere encompassing the sources (arbitrarily taken equal to 1 m); N is the number of terms in the expansion; P_n^m are the Schmidt semi-normalized associated Legendre polynomial functions; and g_n^m and h_n^m are the Gauss coefficients (units of T). The net magnetic moment (m) relates to the first three (n=1) Gauss coefficients as:

$$
m = \frac{4\pi}{\mu_0}a^3\sqrt{\left(g_1^0\right)^2+\left(g_1^1\right)^2+\left(h_1^1\right)^2}
\tag{8}
$$

We can rewrite Equation 7 in matrix form:

$$
\underline{A}\cdot\vec{G} = \vec{B}_{\text{rem}}(r,\theta,\phi)
\tag{9}
$$

where $\vec{B}_{\text{rem}}$ is the remanent field vector of size $n_{\text{obs}}\times 1$ where n_{obs} is the number of observations (three components of the remanent field at each position of the fluxgates), $\underline{A}$ is a matrix of size $3\,n_{\text{obs}}\times N$ that depends on the position of the sensor and the origin (r_0,θ_0,ϕ_0) chosen for the spherical harmonics expansion, and $\vec{G}$ is a vector of size $N\times 1$ containing the Gauss coefficients. The order of the expansion is limited by the amount of data acquired. For five positions of the fluxgate rail, the sensors are collectively located at 20 different positions over the course of one experiment such that $n_{\text{obs}} = 60$. We are in this case limited to an expansion of order $N = 6$ (i.e., 48 Gauss coefficients).

The limited number of observations adds complexity to the inversion problem described by Equation 9. In theory, any magnetic field can be described by an infinite spherical harmonics expansion independent of the choice of the expansion's origin. In typical inversion problems such as determining the net magnetic moment of a planetary body, the abundance and wide spatial coverage of the data makes it possible to set the origin of the expansion (r_0,θ_0,ϕ_0) to the origin of the planetary reference frame (0,0,0). In our case, the choice of an arbitrary origin may not necessarily be compensated with a large amount of data points. To overcome this problem, we solve Equation 9 for $\vec{G}$ for different origins of the expansion. We do so using a nonlinear least square regression with Tikhonov regularization (Hansen, 2001), which finds the origin that minimizes the following constraint:

$$
\|\underline{A}\cdot\vec{G}-\vec{B}\|_2^2 + \lambda^2\|\vec{G}\|_2^2
\tag{10}
$$

where $\|\cdot\|_2^2$ is the L_2 norm squared and λ is a regularization parameter chosen to provide an optimal balance between minimizing the residuals without overfitting of the noise. In practice, the algorithm starts with an initial guess of (0,0,0) for the origin and calculates Equation 10 for a given; it then moves to other origins and recomputes Equation 10 until the origin that minimizes it is found. For a given set of data, the regression is conducted for a wide range of choices of λ (e.g., 10 to 10^5). It is common practice to plot the residuals $\|\underline{A}\cdot\vec{G}-\vec{B}_{\text{rem}}\|_2^2$ as a function of the norm of the solution $\|\vec{G}\|_2^2$ for different λ. If the problem is not too ill-posed, this plot forms a so-called L-curve, where $\|\vec{G}\|_2^2$ first diverges for small residuals, then plateaus as residuals increase. The value of λ corresponding to the "knee" of the curve should offer the best compromise between minimizing $\|\vec{G}\|_2^2$ and $\|\underline{A}\cdot\vec{G}-\vec{B}_{\text{rem}}\|_2^2$. The optimal origin corresponding to this value of λ is then used to calculate the Gauss coefficients (Equation 9) and the magnetic moment (Equation 8).

3.4. Sources of Uncertainty of the Measurements

We identified and quantified whenever possible both random and systematic sources of uncertainty of the system. Random errors can be a consequence of the unshielded environment of the experiment or can be intrinsic to the sensors. The dominant sources of random errors due to the environment are the spatial and temporal variations of the background field. Spatial variations yield a nonuniform background field and therefore a nonuniform applied field throughout the sample, influencing in an unknown fashion the induced component of the sample's field. Spatial variations of the background field at each position of the fluxgates are corrected for when computing $\vec{B}_{\text{sample}}$ from the data acquired with and without the sample inside. Conversely, temporal fluctuations between two measurements repeated with and without the sample will influence $\vec{B}_{\text{sample}}$. We attempted to perform gradiometry measurements to cancel out the background field fluctuations by placing the Bartington fluxgate at >1 m outside the system, oriented along the instrument's reference frame. The distance between the fluxgate and the system had to be sufficiently large such that only the background field is sensed. However, spatial variations of the background field and differences in temporal variations inside and far outside the system were too significant to make effective use of the gradiometry data. Instead, we simply used these data to monitor background field variations to identify extraordinary variations of several μT over >1 min that would require repetition of some of the measurements. The fluxgates are additional sources of random errors due to their frequency-dependent noise (e.g., flicker and white noise) and their digitization noise. The latter relates to the value of the gain used. For a gain of 1, the manufacturer guarantees a resolution of ±25 nT (2 s.d.). No information is given by the manufacturer regarding the flicker noise and white noise.

Systematic errors depend on the MEDA fluxgates and do not significantly vary from one experiment to the other. In our system, we identified three potential sources of systematic errors for the fluxgates: (1) their scale factor uncertainty, (2) their offset, and (3) their orientation uncertainty. Regarding (1), the manufacturer datasheet indicates an accuracy of ±0.25% (2 s.d.) of the measured field. Regarding (2), to quantify the offsets of the fluxgates, we measured the field recorded by each fluxgate placed consecutively inside a permalloy shield in a transformed-steel magnetically shielded room where the ambient field was reduced to <10 nT. The offset of a given component is half the difference between the measured field strength in two opposite directions. The largest offsets found were of the order of ∼10 nT, which is negligible compared to the other identified sources of noise. Regarding 3), the manufacturer datasheet indicates that each of the three sensors (one per axis) inside a fluxgate can be tilted up to 1° (2 s.d.) with respect to the nominal orthogonal reference frame. As a consequence, each measured component could differ by up to $\sin(1°) \sim 2\%$ with respect to its expected value. To verify this value, we built one set of 68.7 cm vertical Helmholtz coils separated by 38 cm with 26 wire turns in the shielded room ($||\vec{B}_{\text{bg}}|| < 100$ nT). We placed consecutively each fluxgate at the center of the system and recorded the field for currents between 0 and 1 A. We subtracted the vertical component of the field at $I = 0$ A (background field) from the measured applied field to obtain the vertical component of the compensation field. This operation was repeated aligning each sensor inside each fluxgate with the coil axis. Comparing the measured values and their simulated counterparts we found that they were all within <2% of each other, validating the 1° precision on the orientation of the sensors. Additional systematic errors were introduced during the assemblage of the instrument. In particular, we estimate a possible misalignment of each fluxgate with respect to the system's reference frame up to 2° (2 s.d.) in the horizontal and vertical planes.

Because we cannot quantify and correct for all systematic errors, the latter may yield a bias in the mean estimate of the magnetic moment. To assess the significance of such bias, we simulated the compensation field generated inside our instrument (same positions of the fluxgates) by a 1.9 cm cube uniformly magnetized along its diagonal with a magnetic moment of 8 A m^2 (adapted from Yang et al., 1990). For simplicity, we assumed the remanent field was directly measured. We sequentially introduced a misalignement of the sensors in each fluxgates and a misalignment of the fluxgates. We used the "measured" field to estimate the magnetic moment (Section 3.3). We found that the misalignments of the sensors inside the fluxgates and of the fluxgates themselves (introduced separately or combined) can create a bias of a few percents in the average estimate of the magnetic moment (Figure 6a). This conclusion was verified on real data acquired on a well-characterized sample (Section 4.2).

Finally, the manual orientation of the whole system along the horizontal component of the background field has an uncertainty of about ±3°. Because of this offset, the orientation of the applied field will vary as the magnitude of the compensation field increases, affecting $\underline{\chi}\hat{r}_{\text{applied}}$ in Equation 6. This effect will not be significant when measuring strong samples with isotropic magnetic susceptibility like a magnet, but should be acknowledged in the case of weaker, anisotropic natural samples such as meteorites. The only way to reduce this uncertainty is to align the background field and the compensation field as closely as possible.

4. Validation: Magnet With Known Magnetic Moment

We tested our protocol using a standard sample with known magnetic moment, a $1.9 \times 1.9 \times 1.9$ cm Nd-Fe-B magnet from K&J Magnetics. The magnetic moment m (A m^2) is approximately equal to $B_r V \mu_0^{-1}$ where B_r (T) is the remanent field and V (m^3) is the volume of the magnet. According to the manufacturer, $B_r = 1.465 \pm 0.015$ T and $V = (6.91 \pm 0.053) \times 10^{-6}$ m^3 (uncertainties are 2 standard deviations, s.d.); therefore $m = 8.05 \pm 0.15$ A m^2. The measurements were conducted in the Massachusetts Institute of Technology Paleomagnetism Laboratory following the protocol detailed in Section 3. Data were acquired for five different positions of the fluxgate rail (Figure 2). The sample was placed on a plexiglass base, centered and held in place with aluminum brackets. The system parameters and sequence of currents are summarized in Table 1.

4.1. Isolation of the Magnet's Remanent Field

The first series of measurements were conducted without the magnet. The Bartington fluxgate placed at the center was used to measure $\vec{B}_{\text{bg}}(t)$ ($I = 0$ A; Figures 4a and 5a–5c) and data acquired by the MEDA fluxgates were concatenated into $\vec{B}_{\text{total}}^{\text{no sample}}(t)$ (Figures 4b and 5a–5c). With the second series of measurements and the magnet inside, we constructed $\vec{B}_{\text{total}}^{\text{with sample}}(t)$. These vectors contain the temporal signals recorded during the one-minute acquisitions for each position of the rail, fluxgate, and current step. From there, we proceeded by bootstrapping. To account for the effect of temporal fluctuations of the background field (∼100 nT; Figures 5a–5c; Section 3.4), we sampled with replacement as many values as there are data points in these

Table 1
System Parameters

Parameter	Value
Size of the z coils (cm)	145
Spacing between z coils (cm)	74
Number of turns in the z coil	18
Size of the x coils (cm)	130
Spacing between x coils (cm)	66
Number of turns in the x coil	10
Spacing between the MEDA fluxgates (cm)	27.95
Position of the center of the magnet (x, y, z) (cm)	(1.27, 0, −1.27)
Position of the Bartington fluxgate at the center (x, y, z) (cm)	(−2.54, 2.54, −0.6)
Height of the fluxgate rail at positions 1, 2, 3, 4, 5 (cm)	10.2, −5.1, 10.2, −5.1, 26.7
Current z coils (A)	0, 0.375, 0.75, 1.125, 1.5, 1.875, 2.255
Corresponding $B_{\text{applied},z}$ (μT)	−45.85, −37.96, −30.06, −22.17, −14.29, −6.42, 1.54
Currents x coils (A)	0, 0.198, 0.395, 0.593, 0.791, 0.989, 1.19
Corresponding $B_{\text{applied},x}$ (μT)	−12.72, −10.14, −7.57, −4.99, −2.41, 0.17, 2.79

Note. The first column lists the parameters and the second column the respective values used in our instrument.
Abbreviation: MEDA, Macintyre Electronic Design Associates.

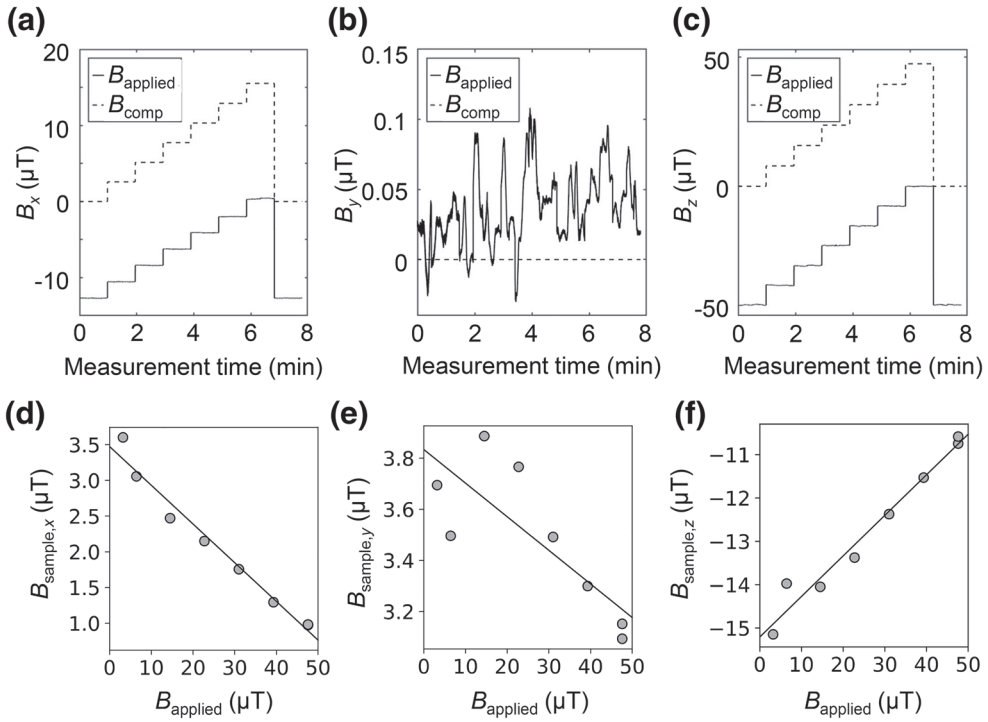

Figure 5. (a–c) Three components of the applied field measured at the center of the system (solid line) and the simulated compensation field (dashed line) as a function of measurement time. The difference between the two curves is the background field (Equation 1). The small delays accumulated between each 30-s acquisition and between each current step are not shown such that the acquisition of this whole sequence took ~30 min. High-frequency (>0.1 Hz) fluctuations are visible in (b) because of the weak values of this field component due the fact that the *y* component of the field is perpendicular to the background field (e.g., Figure 2). (d–f) Three components of the magnet's total field (gray circles) as a function of magnitude of the applied field for fluxgate 7 (Figure 2) with coordinates (−10.2, −43.2, and −5.1) cm. The two data points at maximum applied field correspond to the first and last current steps ($I = 0$ A). The regression line is shown and the components of the magnet's remanent field are the intercepts. The remanent field is an order of magnitude stronger than the induced field, as expected for a magnet. The quasilinear relationship between the sample field components and the magnitude of the applied field support the dipole assumption used in Equation 6.

three raw data vectors and averaged over the acquisition time. From $\vec{B}_{\text{total}}^{\text{no sample}}$ and $\vec{B}_{\text{total}}^{\text{with sample}}$ we calculated $\vec{B}_{\text{sample}}$. To account for the spatial variations of the applied field across the sample—due to the nonzero volume of the sample and the fact that it may be only approximately centered in the system—we randomly chose a point within the volume of the sample and simulated $\vec{B}_{\text{comp}}$ in that point (instead of the center of the system; Figure 4a). We obtained $\vec{B}_{\text{applied}}$ by summing $\vec{B}_{\text{bg}}$ and $\vec{B}_{\text{comp}}$. Finally, we estimated each component of the remanent field at each position of the fluxgates using the intercept of the regression line between the corresponding component of $\vec{B}_{\text{sample}}$ and $\vec{B}_{\text{applied}}$ (Figures 4c and 5d–5f). This sequence of operations was repeated 100 times. The remanent field values were sorted in ascending order with the 2nd and 98th values representing the 95% confidence interval on each component.

4.2. Estimation of the Magnet's Magnetic Moment

Using all remanent field components at all positions of the fluxgates (i.e., a total of 60 values) we applied the multipole inversion of order $N = 6$ solving Equation 9 under the constraint of Equation 10 for different values of λ. We selected the λthat optimally minimized Equation 10 and used the Gauss coefficients to calculate the magnetic moment (Equation 8). This operation was repeated for the 100 values of the remanent field components (Section 4.1). For this sample, the ordinate range of the L-curve (solution norm) is only marginally affected by the choice of λ (Figure 6b). The curve is made of discrete clusters of points as a consequence of the nonlinear search for the origin of the expansion. Both values of λ at the knee and the

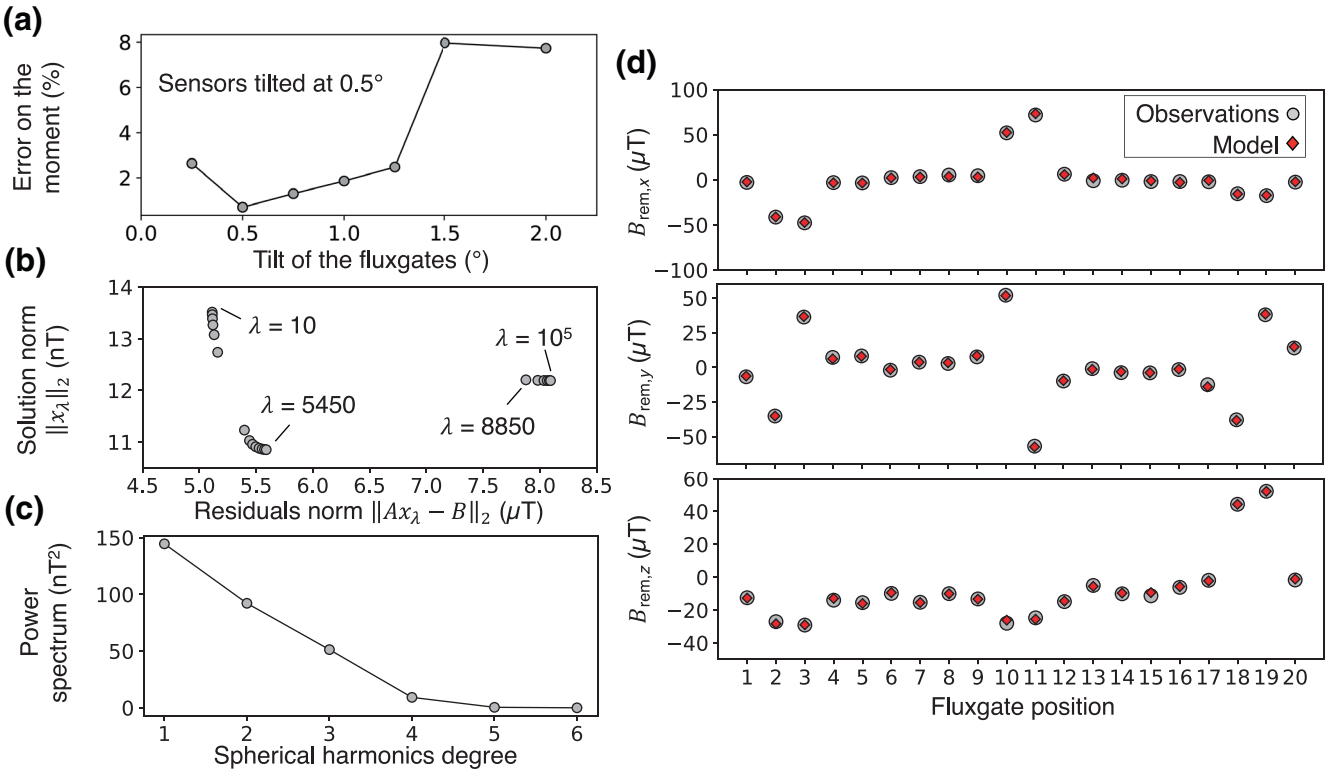

Figure 6. (a) Solution norm as a function of residuals norm (L-curve) for one of the random draws of remanent field components and values of λ between 10 and 10^5. (b) Power spectrum of one solution of the nonlinear least-square regression, obtain with λ = 5,450. (c) Results of simulations showing the effect of systematic errors on the estimate of the magnetic moment. The percentage of error with respect to the nominal magnetic moment is shown as a function of the tilt of the fluxgates, assuming each sensor inside the fluxgates is also tilted by 0.5°. (d) Comparison between observation and model field. The three components of the sample's remanent field are shown for all 20 positions of the fluxgates with the gray circles. The circles are larger than the 95% confidence interval obtained with the bootstrap (not shown here; Section 3.4). The red diamonds show the model field obtained for one draw with λ = 5,450.

first point at the onset of the plateau at higher values of the residuals norm (λ= 5,450 and 8,850 on Figure 6b) yield estimates of the magnetic moment 8.53 ± 0.03 A m^2 (2 s.e.) and 7.66 ± 0.04 A m^2, respectively. These uncertainties only reflect the contribution of the sources of random noise. As expected from our simulations (Section 3.4), the mean estimates are within 5% of the nominal average magnetic moment of the magnet, most likely due to the sources of systematic errors. This value of 5% will be adopted in future measurements to add the contribution of the systematic errors to the total uncertainty of the estimate. In addition, both solutions exhibit a power spectrum that has totally decayed by spherical harmonics degree 6 (Figure 6c), which support the choice of a maximum degree 6 for the inversion. Both model fields can reproduce the observed field (Figure 6d). This demonstrates that the magnetometer array can be confidently used to estimate the magnetic moment of a sample.

5. Magnetic Measurements of an Iron Meteorite

This instrument was primarily developed to estimate the magnetic moments of large iron meteorites. As an example of such an application, we present results obtained for the Casas Grandes IIIAB iron meteorite (~0.6 × 0.5 × 0.45 m, 750 kg, USNM 369-2) measured at the Smithsonian Museum of Natural History's storage facility (Suitland, MD). The system parameters are given in Table 2. The total volume of equipment was ~2 m^3 and weighted > 100 kg. Assembling and aligning the system took 6.5 h. The system was placed near the center of an empty, ~8 × 8-m area, as far as possible from stray sources of magnetic fields (computer at ~3 m, metallic shelves at ~4 m and outdoor parking at ~10 m). The series of measurements (with and without the meteorite) consisted of seven current steps (including the first and last steps at $I = 0$ A; Table 2) and five positions of the rail (Figure 2); they each lasted ~2.5 h. We conducted two series without the meteorite. Between them, the meteorite was brought with a forklift and visually centered inside the system (Figure 2c).

Table 2
System Parameters

Parameter	Value
Size of the z coils (cm)	249
Spacing between z coils (cm)	142
Number of turns in the z coil	27
Size of the x coils (cm)	233
Spacing between x coils (cm)	134
Number of turns in the x coil	16
Spacing between the MEDA fluxgates (cm)	34
Position of the center of the meteorite (x, y, z) (cm)	(10, 2.5, 0.5)
Position of the Bartington fluxgate at the center (x, y, z) (cm)	(−2.4, 0.8, 1.2)
Height of the fluxgate rail at positions 1, 2, 3, 4, 5 (cm)	29.7, −16.0, 29.7, −16.0, 60.2
Current range in z coils and x coils (A)	0–2.5 and 0–2.285
Range of $B_{\text{applied},z}$ and $B_{\text{applied},x}$ (μT)	−45.5 to −2.6 and 24.8 to 0.17

Note. The first column lists the parameters and the second column the respective values used in our instrument.
Abbreviation: MEDA, Macintyre Electronic Design Associates.

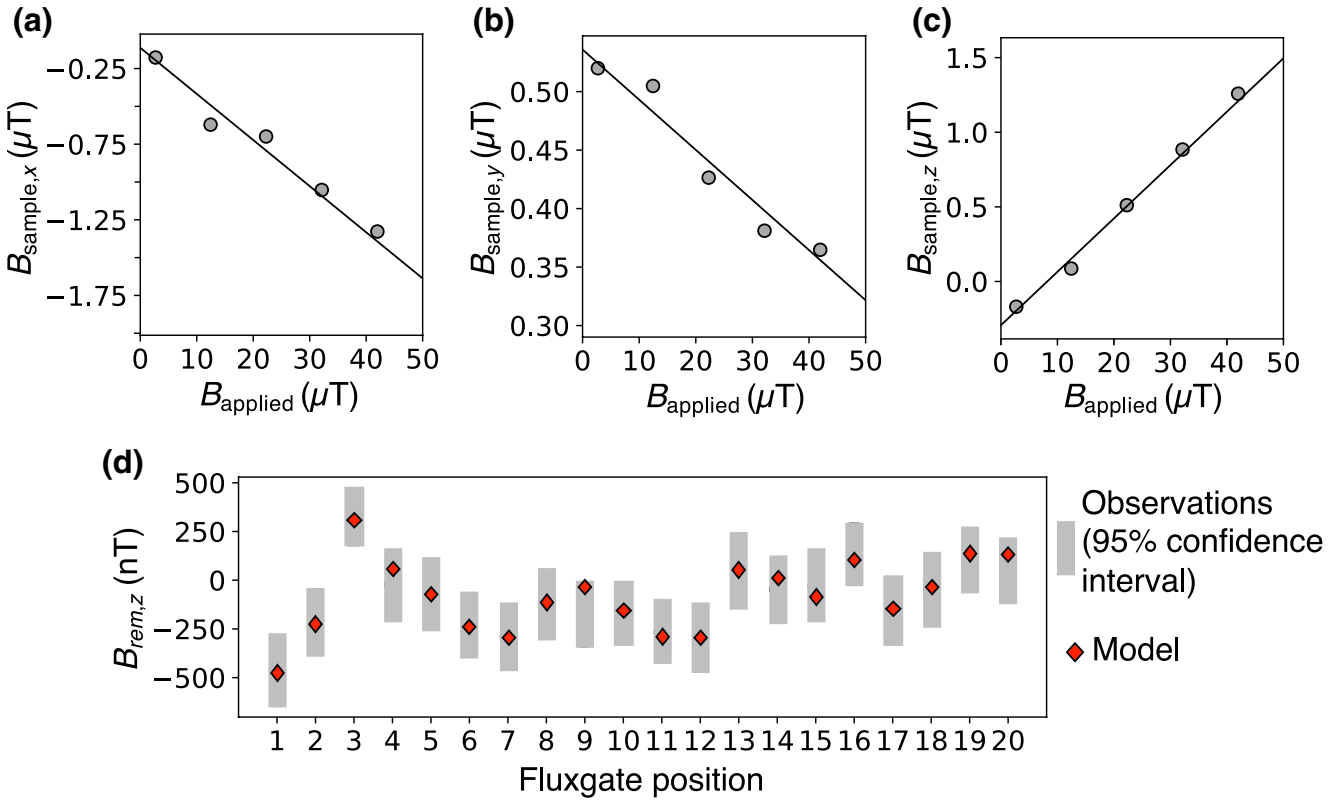

Figure 7. (a–c) Three components of the Casas Grandes iron meteorite's total field (gray circles) as a function of magnitude of the applied field for the fluxgate 7 (Figure 2) with coordinates (17.9, −78.7, and −16.0) cm. The two data points at maximum applied field correspond to the two measurements at zero compensation field acquired at $I = 0$ A. The regression line is shown. Unlike the magnet, induced and remanent fields are of the same order of magnitude. (d) Comparison between observation and model field. The 95% confidence intervals obtained with the bootstrap (Section 3.4) for the three components of the sample's remanent field are shown for all 20 positions of the fluxgates with the gray bars. The red diamonds show the model field obtained for one of the random draws of the remanent field components.

Safety rules of the museum imposed that the meteorites stayed on their wooden sustaining pallet. We added several plastic pallets to center the meteorite vertically. Some of the sustaining pallets had a few metallic nails, but given the distance between the nails and the fluxgates, these did not have any influence on the measurements.

Compared to the measurements of the magnet, two sources of uncertainty were more prominent: (1) the spatial fluctuations of the background field within the sample given the large volume of the meteorite and (2) the effect of the anisotropy of the magnetic susceptibility, likely stronger for such a large natural sample due to the misalignment (±3°) of the system's axes with the background field. The effect of source (1) was accounted for in the bootstrap procedure (Section 3.4) where we simulate the compensation field at a random point within the meteorite's volume and use it to estimate $\vec{B}_{\text{applied}}$. For a misalignment of the system within ±3°, up to sin(3°)∼5% of the applied field is projected onto another axis. However, because the anisotropy of the susceptibility is unknown (Section 3.2), we could not correct for this effect in the post-processing of the data. We find that the model field falls within all the 95% confidence intervals of the data (Figure 7). This implies that a 6th order multipole inversion model was sufficient to explain the data given the level of uncertainties. As a result, we find that the magnetic moment of Casas Grandes is 0.5 ± 0.3 A m^2 (2 s.e.). Note that we do not fit for the magnetization distribution within the sample and only recover the magnitude of the net magnetic moment. This is because our objective is to constrain the dependence of the magnetization intensity as a function of meteorite volume over several orders of magnitude of the radius.

6. Conclusion

We developed a portable magnetometer array and associated data processing to measure the remanent magnetic field of meter-size meteorites and estimate their magnetic moments. A two-axis square Helmholtz coil system enables control of the field applied to the meteorite and four three-axis fluxgate magnetometers measure the total field inside the system at multiple positions. Measurements are conducted at different strengths of the applied field. To isolate the remanent component of the sample's total field from its induced component, we characterize the field of the sample as a function of the magnitude of the applied field. A least squares regression to these data provides the sample's field at zero applied field corresponding to its remanent component. We use a multipole inversion to estimate the net magnetic moment from the remanent field measured at different positions occupied by the fluxgate sensors. The system enables retrieval of the magnetic moment of a well-characterized sample within 5% of its nominal value. It has been used to estimate the magnetic moment of a 750 kg iron meteorite. This versatile instrument and data processing can easily be adapted to analyze samples with different sizes.

Acknowledgements
We thank Tim McCoy and Julie Hoskin for granting us access to the Smithsonian Museum of Natural History's meteorite collection and the logistics team (Richard Stoyer and Daniella Haigler) for their invaluable assistance during the measurements. We thank Kathryn Rowe, Henry Gonzalez, and Roger Fu for loaning us their MEDA fluxgate magnetometers. We thank Pablo Narvaez for helpful discussions about magnetic measurements of large samples. We thank the MIT International Science and Technology Initiatives (MISTI) for support. Elise Clavé, Clara Maurel, and Benjamin P. Weiss thank the NASA Discovery Program (grant NNM16AA09C) and T. F. Peterson, Jr. for support. Eduardo A. Lima and Benjamin P. Weiss thank the National Science Foundation (grant DMS-1521765) for support. Elise Clavé thanks the Fondation ISAE-SUPAERO for support. Raw data and Python source code for this work are publically available at https://dspace.mit.edu/handle/1721.1/125696

References

Asphaug, E., & Reufer, A. (2014). Mercury and other iron-rich planetary bodies as relics of inefficient acrretion. *Nature Geoscience*, *7*, 564–568.

Biersteker, J. B., Weiss, B. P., Heinisch, P., Herčik, D., Glassmeier, K.-H., & Auster, H.-U. (2019). Implications of Philae magnetometry measurements at comet 67P/Churyumov–Gerasimenko for the nebular field of the outer solar system. *Astrophysical Journal*, *875*, 39.

Buchwald, V. F. (1975). *Handbook of Iron Meteorites*. New York: University of California Press.

Cain, J. C., Hendricks, S. J., Langel, R. A., & Hudson, W. V. (1967). A proposed model for the international geomagnetic reference field-1965. *Journal of Geomagnetism and Geoelectricity*, *19*(4), 335–355.

Elkins-Tanton, L. T., Asphaug, E., Bell, J. F., Bercovici, D., Bills, B. G., Binzel, R. P., et al. (2017). Asteroid (16) Psyche: Visiting a metal world. Abstract 1718. *Lunar Planetary Science Conference*, *48*, The Woodlands, TX.

Elkins-Tanton, L. T., Asphaug, E., Bell, J. F., Bercovici, H., Bills, B., & Binzel, R., et al. (2020). Observations, meteorites, and models: A pre-flight assessment of the composition and formation of (16) Psyche. *Journal of Geophysical Research: Planets*, *125*, e2019JE006296.

Ermakov, A. I., Park, R. S., & Bills, B. G. (2018). Power laws of topography and gravity spectra of the solar system bodies. *Journal of Geophysical Research: Planets*, *123*(8), 2038–2064. https://doi.org/10.1029/2018je005562

Fuller, M., Goree, W. S., & Goodman, W. L. (1985). An introduction to the use of SQUID magnetometers in biomagnetism. In J. L. Kirschvink, D. S. Jones & B. J. MacFadden (Eds.), *Magnetite Biomineralization and Magnetoreception in Organisms* (pp. 103–151). Boston, MA: Springer.

Gattacceca, J., Rochette, P., Denies, M., Consolmagno, G., & Folco, L. (2005). An impact origin for the foliation of chondrites. *Earth and Planetary Science Letters*, *234*(3-4), 351–368. https://doi.org/10.1016/j.epsl.2005.03.002

Hansen, P. C. (2001). The L-curve and its use in the numerical treatment of inverse problems. In P. Johnson (Ed.), *Computational Inverse Problems in Electrocardiology* (pp. 119–142). WIT Press.

Kirschvink, J. L. (1992). Uniform magnetic fields and double-wrapped coil systems: Improved techniques for the design of bioelectromagnetic experiments. *Bioelectromagnetics*, *13*, 401–411.

Mehlem, K. (1978). Multiple magnetic dipole modeling and field prediction of satellite. *IEEE Transactions on Magnetics*, *14*, 1064–1075.
Misakian, M. (2000). Equations for the magnetic field produced by one or more rectangular loops of wire in the same plane. *Journal of Research of the National Institute of Standards and Technology*, *105*, 557–564.
Neufeld, J. A., Bryson, J. F. J., & Nimmo, F. (2019). The top-down solidification of iron asteroids driving dynamo evolution. *Journal of Geophysical Research: Planets*, *124*, 1331–1356.
Polanskey, C. A., Marsh, D. M., Moore, et al. (2018). Psyche science operations concept: Maximize reuse to minimize risk. *International Conference on Space Operations*, *15*, Marseille, France.
Shepard, M. K., Richardson, J., Taylor, P. A., et al. (2017). Radar observations and shape model of asteroid 16 Psyche. *Icarus*, *281*, 388–403.
Tauxe, L., Banerjee, S. K., Butler, R. F., & van der Voo, R. (2018). *Essentials of Paleomagnetism* (5th web edition). University of California Press.
Terho, M., Pesonen, L. J., & Kukkonen, I. T. (1993). The petrophysical classification of meteorites: New results. *Geological Survey of Finland Report Q29.1/91/1*, 1–68.
Uehara, M., Gattacceca, J., Quesnel, Y., Lepaulard, C., Lima, E. A., Manfredi, M., & Rochette, P. (2017). A spinner magnetometer for large Apollo lunar samples. *Review of Scientific Instruments*, *88*, 104502.
Wasilewski, P. J., Acuña, M. H., & Kletetschka, G. (2002). 433 Eros: Problems with the meteorite magnetism record in attempting an asteroid match. *Meteoritics & Planetary Science*, *37*(7), 937–950. https://doi.org/10.1111/j.1945-5100.2002.tb00868.x
Weiss, B. P., Gattacceca, J., Stanley, S., Rochette, P., & Christensen, U. R. (2010). Paleomagnetic records of meteorites and early planetesimal differentiation. *Space Science Reviews*, *152*(1-4), 341–390. https://doi.org/10.1007/s11214-009-9580-z
Weiss, B. P., Lima, E. A., Fong, L. E., & Baudenbacher, F. J. (2007). Paleomagnetic analysis using SQUID microscopy. *Journal of Geophysical Research*, *112*. https://doi.org/10.1029/2007jb004940
Yang, Z. J., Johansen, T. H., Bratsberg, H., Helgesen, G., & Skjeltorp, A. T. (1990). Potential and force between a magnet and a bulk $Y_1Ba_2Cu_3O_7$-δ superconductor studied by a mechanical pendulum. *Superconductor Science and Technology*, *3*(12), 591–597.